NIST Internal Report
NIST IR 8582

# Priming Additively Manufactured Cobalt-free Maraging Steels for Improved Properties through Changes to As-Built Microstructure

Alec I. Saville
Jake T. Benzing
Fan Zhang
Joseph W. Aroh
Jordan S. Weaver
R. Colby Evans
Nicholas Derimow
Samantha Webster
Nik W. Hrabe
Cassidy R. Allen
Newell Moser
May L. Martin
Jason Holm
Christin Aumayr
Tilman Seifert
Michael Hirtler

This publication is available free of charge from:
https://doi.org/10.6028/NIST.IR.8582

NIST NATIONAL INSTITUTE OF STANDARDS AND TECHNOLOGY
U.S. DEPARTMENT OF COMMERCE

**NIST Internal Report**
**NIST IR 8582**

# Priming Additively Manufactured Cobalt-free Maraging Steels for Improved Properties through Changes to As-Built Microstructure


Alec I. Saville, Jake T. Benzing, R. Colby Evans, Nicholas Derimow, Nik Hrabe, Newell Moser, May L. Martin, Jason Holm
*Applied Chemicals and Materials Division*
*Material Measurement Laboratory*

Fan Zhang, Joseph W. Aroh
*Materials Measurement Science Division*
*Material Measurement Laboratory*

Jordan Weaver
*Intelligent Systems Division*
*Engineering Laboratory*

Samantha Webster
*Materials Science and Engineering Division*
*Material Measurement Laboratory*

Christin Aumayr,Tilman Seifert, Michael Hirtler
*voestalpine BÖHLER Edelstahl, Austria*

Cassidy Allen
*Applied Chemicals and Materials Division*
*Material Measurement Laboratory*
*College of Engineering and Applied Science*
*University of Colorado Boulder*



This publication is available free of charge from:
https://doi.org/10.6028/NIST.IR.8582

July 2025




U.S. Department of Commerce
*Howard Lutnick, Secretary*

National Institute of Standards and Technology
*Craig S. Burkhardt, Acting NIST Director and Under Secretary of Commerce for Standards and Technology*

NIST IR 8582
July 2025

Certain equipment, instruments, software, or materials, commercial or non-commercial, are identified in this paper in order to specify the experimental procedure adequately. Such identification does not imply recommendation or endorsement of any product or service by NIST, nor does it imply that the materials or equipment identified are necessarily the best available for the purpose.



**Publication History**
Approved by the NIST Editorial Review Board on 2025-05-28

**How to Cite this NIST Technical Series Publication**
Alec I. Saville, Jake T. Benzing, Fan Zhang, Joseph W. Aroh, Jordan S. Weaver, R. Colby Evans, Nicholas Derimow, Samantha Webster, Nik Hrabe, Cassidy R. Allen, Newell Moser, May L. Martin, Jason Holm, Christin Aumayr, Tilman Seifert, Michael Hirtler, (2025) Priming Additively Manufactured Cobalt-free Maraging Steels for Improved Properties through Changes to As-Built Microstructure. (National Institute of Standards and Technology, Gaithersburg, MD), NIST Internal Report (IR) NIST IR 8582. https://doi.org/10.6028/NIST.IR.8582

**Author ORCID iDs**
Alec Saville: 0000-0001-9245-7056
Jake Benzing: 0000-0002-7266-870X
Fan Zhang: 0000-0003-1248-0278
Jordan Weaver: 0000-0003-4857-5164
R. Colby Evans: 0000-0002-2134-238X
Nicholas Derimow: 0000-0001-7526-1836
Nik Hrabe: 0000-0001-7585-0980
Newell Moser: 0000-0002-3346-6427
May L. Martin: 0000-0002-5153-9597

**Contact Information**
jake.benzing@nist.gov

## Abstract

Supply chain challenges and health concerns have prompted the development of new cobalt-free, chromium-containing maraging steels, with several new alloys already commercialized. These alloys offer a more economical alternative to the currently used cobalt-containing maraging steels, identified as C300 and C350. However, cobalt-free, chromium-containing maraging steels exhibit lower strengths after heat treatment compared to the existing cobalt-containing alloys. To enable their replacement with maintainable alternatives, new processing pathways are necessary to create microstructures that can match the performance of current cobalt-containing or titanium-strengthened maraging steels. This study investigates the effects of varying the laser beam powder bed fusion (PBF-LB) build parameters on the cobalt-free, chromium-containing maraging steel M789 to modify the as-built microstructure. The goal is to find new ways to achieve equivalence with the existing cobalt-containing maraging steels. Modeling the PBF-LB build process indicates significant changes in thermal history, which could lead to unique developments in solidification and solid-state microstructures. However, characterization of the as-built material revealed little to no influence of the build parameters on the solid-state or solidification microstructures. This suggests that M789 and similar alloys undergo phase transformations that are resilient to variations in build parameters. Additionally, further research is warranted to better understand the solid-state transformations of M789, particularly regarding its resistance to changes in build parameters and the development of other additive manufacturing-resilient alloys.

## Keywords

Additive Manufacturing; Cobalt-free Maraging Steels; Laser Powder Bed Fusion; Microstructure; Tensile Properties

## Table of Contents

## 1. Introduction

Maraging steels are a class of high-performance iron-based (Fe) alloys used extensively in applications requiring high strength-to-weight ratios, thin structural cross-sections, or high toughness [1–5]. Example uses include rocket motor casings, load cells, torsion-bar suspensions, aircraft landing gear, manufacturing tooling (dies and molds), and bearings. Most applications stem from the combination of strength and toughness maraging steels exhibit [2,4,5].

These desirable properties originate from the two-step processing route of these alloys. Maraging steels are first solutionized and quenched to form a martensitic matrix [6,7]. This "soft" martensite is subsequently hardened via precipitation heat treatment to create dispersed, fine precipitate phases and establish short and/or long-range atomic ordering [8,9]. This two-step process of "martensite aging" creates microstructures with high strength, high ductility (relative to the strength of the alloy), and thereby high toughness. Achieving these performance characteristics require a series of specific alloying elements. High nickel (Ni) contents, often greater than 10 wt. % to 15 wt. %, are required to readily form a martensitic matrix in traditional processing routes. For example, the widely used C300 maraging steel (also identified as M300) uses 18 wt. % Ni. Ni is also a core component in several precipitates in maraging steels, commonly with a Ni3X stoichiometry [10,11].

Traditional maraging steels also require ~ 10 wt. % cobalt (Co) and ~ 5 wt. % molybdenum (Mo) to achieve maximum precipitation strengthening. Co and Mo exhibit a synergistic effect with each other, drastically increasing the precipitation strengthening of Mo-based precipitates in martensite [12,13]. Individually adding Co or Mo does not produce nearly the same strengthening effect. Ti and Al are often added as supplemental precipitate forming elements, but in quantities far smaller than Ni, Co, or Mo. Ti is known to have a weaker, secondary effect in improving Mo precipitation, but still establish considerable strengthening comparable to Co-additions. Because of this, Ti is the primary precipitate element in the Co-free T-series maraging steels [13].

This combination of core alloying elements creates challenges for using maraging steels. Co and Mo are costly, with market prices ranging from $24,300 to $82,000 and $44,300 to $83,770 per metric ton, respectively, over the last 2 years at the time of writing in late 2024 (according to the London Metal Exchange). These two elements are the most expensive alloying additions in maraging steels, dwarfing the cost of $15,800 to $43,000 per metric ton for Ni. Such prices economically restrict maraging steels to only the most-critical applications and prevent many industries from cost-effectively utilizing the engineering potential of these alloys. Reliably sourcing Co is also problematic. Nearly 75% of the Co mined in 2023 originated from the Democratic Republic of Congo, making Co effectively sourced from a single country [14]. Geopolitical and supply chain risks mean the loss of Co from Congo would prevent critical industries from functioning across the globe. This is further compounded by the increased use of Cobalt in electric vehicles and energy storage applications, putting additional strain on this fragile supply chain.

In recognition of these risks, the United States Geological Survey (USGS) has designated Co as a critical mineral to incentivize contingencies for economic resilience in the case of restricted Co access [15]. In response to growing concerns about occupational exposure to hazardous substances, the European Union adopted Directive (EU) 2022/431, which amends Directive 2004/37/EC on the protection of workers from the risks related to exposure to carcinogens or mutagens at work. Among its provisions, the Directive mandates that the European Commission propose, where appropriate, occupational exposure limits for cobalt and inorganic cobalt compounds. These proposed limits are to be grounded in the latest scientific evidence and developed in consultation with relevant stakeholders [16].

These challenges are not exclusive to the present day. Prior work in the 1980's evaluated the metallurgical impact of removing Co from maraging steels in response to supply chain shocks. Sha et al. analyzed the commercial Co-free, Ti-precipitation strengthened alloy T300 and observed a considerable reduction in Fe-Mo based precipitation [10]. Hickey et al. found this change had negligible impacts on the mechanical properties of T300 when compared to C300 series alloys [12,17]. This finding was attributed to Ti creating sufficient Ni3Ti and Fe-Mo precipitates to generate equivalent strengthening. However, the Co-free alloys had reduced corrosion resistance with respect to the Co-containing alloys, potentially limiting their applications. T-series maraging steels have lagged C-series alloys in application for unclear reasons, meaning the economic resiliency provided by their metallurgical constituency has not been realized yet.

Additionally, recent supply chain disruptions combined with the European Chemicals Agency's (ECHA) classification of cobalt (Co) as a carcinogenic substance have intensified regulatory pressure to eliminate cobalt from alloy formulations [18]. This has, in turn, driven the development of a second generation of cobalt-free maraging steels, which differ from alloys like T300 in that they contain appreciable amounts of chromium (Cr), making them more corrosion resistant than existing maraging steels [19,20]. Example alloys in this space include M789 and Mar-50. However, Cr additions restrict the formation of the Fe-Mo precipitates seen in C300 and T300 alloys, forming instead G-phase precipitates ($Ni_{16}Ti_6Si_7$) [21–24]. The G-phase provides less strengthening compared to Fe-Mo precipitates, leading to reduced strengths but increased ductility for the second generation of Co-free maraging steels.

Existing engineering designs using maraging steels expect the high strength of Co-containing maraging steels. Thus, the strength debit from adding Cr prevents the immediate adoption of new Co-free maraging steels despite the cost and safety benefits. New metallurgical processing routes are needed to increase the strength of Co-free, Cr-containing maraging steels. Additive manufacturing (AM) is one such route. The rapid solidification, non-equilibrium partitioning, unique phase transformations, and thermal cycling of AM builds are new processing avenues to create novel microstructures able to boost the performance of Co-free, Cr-containing maraging

steels. Many second-generation Co-free maraging steels were made to create custom tooling via metal AM, implying that a robust commercial supply already exists for these materials.

This study lays the groundwork towards reaching performance parity between both Co-free, Cr-containing alloys, and their Co-containing, Cr-free counterparts. Here, AM builds of the new Co-free maraging steel, M789, are manufactured to identify the most desirable processing parameters towards this goal. Changes in solidification conditions and solid-state microstructure, were experimentally measured. Mechanical properties of as-built material for each tested parameter set were also measured. This research focuses on identifying the unique attributes of each as-built microstructure that could potentially provide a pathway to improve the performance of Co-free, Cr-containing alloys, or prime the alloy for improved properties via post-build heat treatments.

## 2. Experimental Methods

### 2.1. Sample Preparation

One laser beam powder bed fusion (PBF-LB) build of the Co-free, Cr-containing M789 maraging steel was manufactured on an EOS M290. The powder batch composition and as-built compositions are included in Table 1 from inductively coupled plasma mass spectrometry (ICPMS) measurements. Phosphorous and sulfur content was less than 0.005 wt. % and 0.001 wt. %, respectively, in both measurements. M789 powder consisted of particles nominally 15-45 µm in diameter, with a D90 of 45 µm.

**Table 1: ICPMS determined compositions for the M789 powder and as-built material.**

| Condition | Fe (wt. %) | Cr (wt. %) | Ni (wt. %) | Ti (wt. %) | Al (wt. %) | Si (wt. %) | C (wt. %) |
|---|---|---|---|---|---|---|---|
| Powder | 75.68 | 12.28 | 10.06 | 1.00 | 0.55 | 0.42 | 0.013 |
| As-Built | 75.64 | 12.31 | 10.23 | 0.97 | 0.52 | 0.32 | 0.010 |

Five different parameter sets were selected to modify the as-built microstructural evolution and identify pathways to improved material properties (Table 2). Large changes in thermal history were desired to maximize the difference in phase transformations and solute partitioning, both in solidification and the solid state. Parameter sets A & E are identical to recommended M789 build parameters apart from a scan rotation of 67° and 90° respectively. The 67° scan rotation is meant to reduce crystallographic texture, and the 90° scan rotation was chosen to promote a more crystallographically textured solidification microstructure. Here, we note the recommended scan rotation is 47°, and the recommended hatch spacing is 95 µm using EOSPRINT 2.9 software. An older version of printing preparation software (EOSPRINT 1.9) was used in this study. This older version has less rules and parameters for scan rotation angle so the most common scan rotation for older material parameter sets was chosen (67°), and this version only allows hatch spacing to the nearest tens of micrometers so the value was rounded up to 100 µm.

**Table 2: Build parameters used in this study.**

| Parameter Set | Laser Power (W) | Velocity (mm/sec) | Hatch Spacing (µm) | Scan Rotation (°) | Volumetric Energy Density (J/mm$^3$) |
|---|---|---|---|---|---|
| **A** | 370 | 800 | 100 | 67 | 81 |
| **B** | 370 | 500 | 100 | 67 | 112 |
| **C** | 370 | 1200 | 100 | 67 | 64 |
| **D** | 295 | 960 | 100 | 67 | 86 |
| **E** | 370 | 800 | 100 | 90 | 81 |

Specimen manufacturing employed a 1045 steel build plate, an 80 °C build plate heating, 60 µm layer thickness, ceramic recoating blade, grid nozzle, and an argon gas environment. Build

specimens consisted of cubes measuring 20 mm × 20 mm × 20 mm and were removed from the build plate by wire electrical discharge machining (wire-EDM). An illustration of build position and specimen geometry are included in Figure 1A & B for specimens from each build parameter set. 15 mm of each cube was reserved to extract 10× mini-tensile specimens via wire-EDM with the geometry shown in Figure 1C. The majority of A specimens were printed for a future study focused on post-process heat treatments.

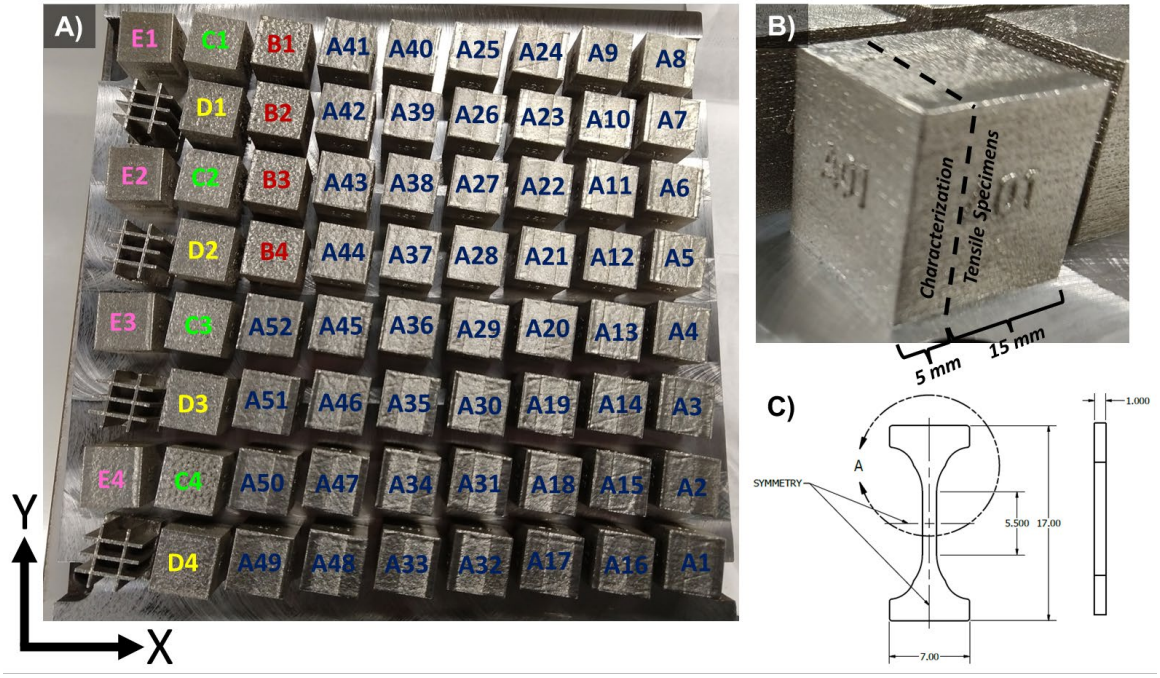


**Figure 1. A) M789 build layout employed in this work. Specimens manufactured using different parameter sets are labelled according to Table 2. Thin-walled structures are included in this graphic but not the focus of this work. B) Sectioning plan for both characterization witness samples and mini-tensile mechanical testing specimens from each block. C) Mini-tensile geometry used to evaluate as-built mechanical properties (dimensions in mm).**

## 2.2. Thermophysical modeling

Thermophysical simulations of each build parameter set were completed using data from the Thermo-Calc TCFE10 + MOBFE5 databases and imported into the Additive Manufacturing module to simulate steady state build conditions. A multicomponent simulation using the theory from Gäumann [25] and modifications by Kurz, Giovanola, and Trivedi (KGT) [26] was also completed to predict the solidification pathway for M789 as a function of solidification velocity using data from the TCFE10 + MOBFE5 databases.

## 2.3. Characterization

The A1, B1, C1, D1, and E1 specimens from Figure 1A were selected for characterization and mechanical properties measurements in this work. All characterization witness samples were ground using 600, 800, and 1200 grit (CAMI scale), rough polished using 9 µm diamond solution, and final polished with 0.05 µm colloidal silica on a vibratory polisher for 24 hours.
Scanning electron imaging (SEM) using secondary electron (SE) and backscatter electron (BSE) detectors was completed using 5 keV and 0.8-6.4 nA. Exploratory scanning transmission electron microscopy (STEM) was completed on focused ion beam (FIB) liftouts using 30 keV and 0.8 nA currents to better understand small-scale features in as-built microstructures. Energy dispersive spectroscopy (EDS) was used to check for partitioning in as-built microstructures and completed using 30 keV and 6.4 nA.

Electron backscattered diffraction (EBSD) mapping of as-built microstructures was completed over areas larger than 2 x 2 mm to obtain close-to-representative orientation data and grain structure. EBSD data processing and parent grain reconstruction was completed using TSL OIM version 9 and the MATLAB plugin MTEX version 5.11.2 in MATLAB 2023b. EBSD step sizes ranged from 30 nm to 100 nm. A 5° grain misorientation threshold and removal of data points with less than 0.1 confidence index (CI) was applied to all data sets. Parent phase reconstructions were completed using TSL OIM V9 and iterative orientation relationships with a 5° tolerance angle, minimum probably ratio of 1.3, variant based parent orientation assignment, 3 orientation averaging iterations, and the removal of any parent grains less than 2 percent of the calculated average size.

Phase identification was completed using X-ray diffraction (XRD) on a Bruker D8 Eiger area detector with a 1 mm diameter beam, 1.5418 Å wavelength, angular step size of 0.02°, 0.25 s dwell time, and a copper (Cu) tube source with a Cu Kα2 filter equipped. Rietveld refinement using the General Structure and Analysis System (GSAS) II program was completed using established best practices to estimate phase fractions [27].

## 2.4. Mechanical Testing

Vickers hardness testing of as-built microstructures was completed using 1 kg of force, 15 s dwell time, 300 µm spacing, and 20 indents per parameter set on fully polished specimens.
Tensile properties of as-built microstructures were measured using an extensometer instrumented load frame under quasi-static strain rates ($10^{-3}$ $s^{-1}$) and a custom tensile geometry based closely on ASTM standard designs depicted in Figure 1C [28]. The load frame employed here was validated in prior testing and used a 3 mm physical extensometer gauge length in ambient conditions. Post-uniform elongation is artificially inflated due to the reduced specimen conditions compared to those employed in ASTM-E8. Nine tensile specimens were run per parameter set, and any specimens which failed outside the extensometer gauge length or near the extensometer pins were excluded. Work hardening rates and exponents were calculated using the process outlined in [29].

# 3. Results and Discussion

## 3.1. Solidification simulations

The addition of Cr to M789 may result in a solidification pathway like conventional stainless steels. To better understand these potential changes and identify desirable phenomena for improved performance of M789, rapid solidification simulations of the AM build process were completed. This consisted of two parts: simulations of dendrite solidification temperature as a function of solidification velocity, and thermophysical melt pool simulations of each parameter set to elucidate changes in thermal history.

### 3.1.1. Dendrite solidification

Theoretical solidification temperatures for the primary solidification phases in M789 (δ-ferrite and γ-austenite) are presented in Figure 2 across a range of solidification velocities. Both phases are expected to have similar liquidus and solidus temperatures irrespective of how fast solidification is occurring. Dendrite tip temperature predictions also show both phases solidify at nearly the same temperature, suggesting M789 solidifies as both δ-ferrite and γ-austenite, irrespective of solidification velocity.

These predictions also suggest the Ni and Cr content of M789 produces a complex, multi-phase solidification process which could be modified by changing build parameters. In many regards, M789's composition is predicted to be an inflection point between δ-ferrite and γ-austenite solidification, analogous to the way stainless steel alloys can also change the primary solidification phase depending on local thermal conditions [30,31]. Local heterogeneities may preferentially promote the solidification of one phase over the other and suggests significant differences in as-built M789 microstructures should be observed across the parameter sets employed here.

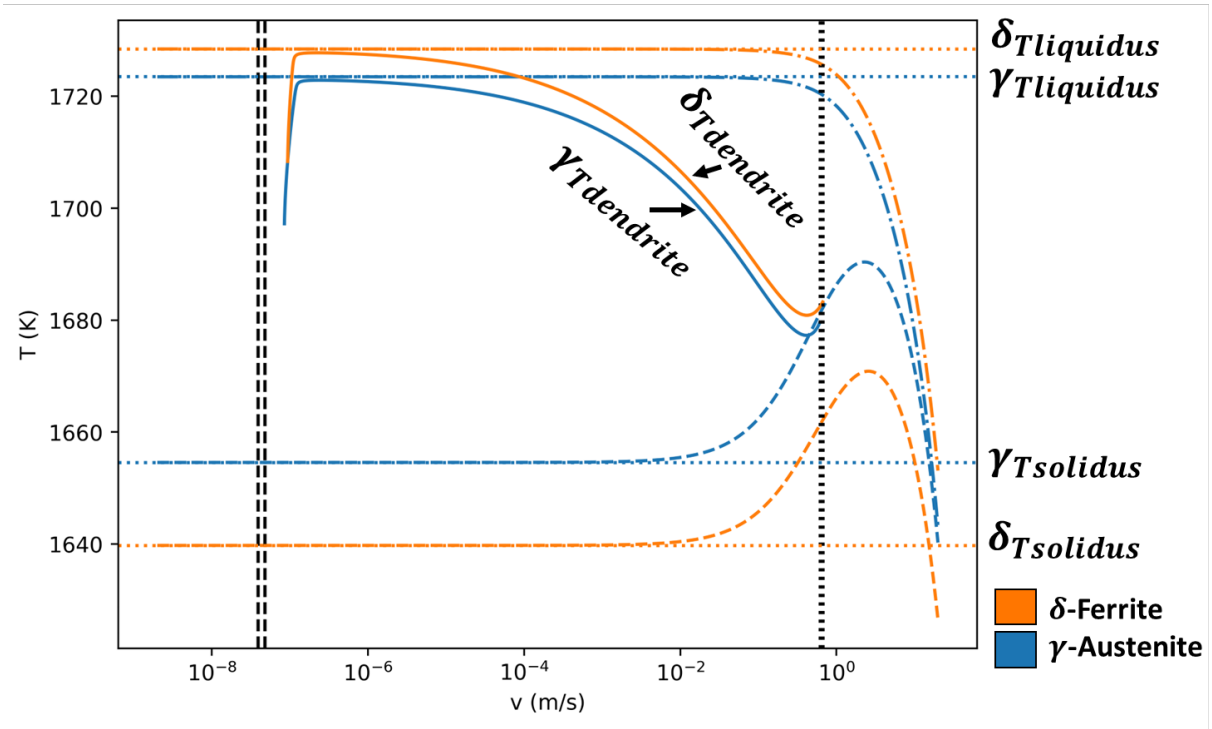


**Figure 2: KGT simulation predicting the dendrite solidification temperatures for δ-ferrite and γ-austenite over a range of solidification velocities. Liquidus and solidus temperature variability with solidification velocity is also included for both phases.**

### 3.1.2. Single raster tracks

Single raster track simulations of each parameter set in Table 2 are presented in Figure 3. The same simulation was used for parameter sets A & E due to only the scan rotation changing between each set. Figure 3 shows each parameter set has a significant impact on the thermal history during the PBF-LB build process. Parameter sets A & E are predicted to produce melt pools ~2× larger than C & D and ~4× smaller in depth than parameter set B. Parameter set B also exhibits the largest mixed liquid-solid volume due to its reduced scanning velocity, enabling the greatest elemental partitioning during solidification of all five conditions. Melt pools for parameter sets C & D are nearly identical despite the different laser power and scan velocities, suggesting these builds should exhibit limited solute partitioning and have similar solidification microstructures. Melt pool geometries are estimates used only for highlighting qualitative trends between each parameter set.

These predictions show changing M789 build parameters is likely to produce significantly different solidification microstructures. Though solidification velocity is predicted to have a negligible effect on the as-solidified microstructure (Figure 2), large changes in thermal gradients within the melt pools are expected to lead to changes in the as-solidified, and likely, solid-state microstructures [30].

Characterization of the as-built microstructures is thus needed to elucidate exactly how each parameter affects microstructural evolution. It should be stressed these simulations were completed only to assess how different the as-built microstructures are, and not quantifiably track or explain observed phenomena. Processes of interest are highlighted in this section, but only to highlight avenues for microstructural control. Future work in phase field simulations would complement these findings greatly and provides rich potential for future work.

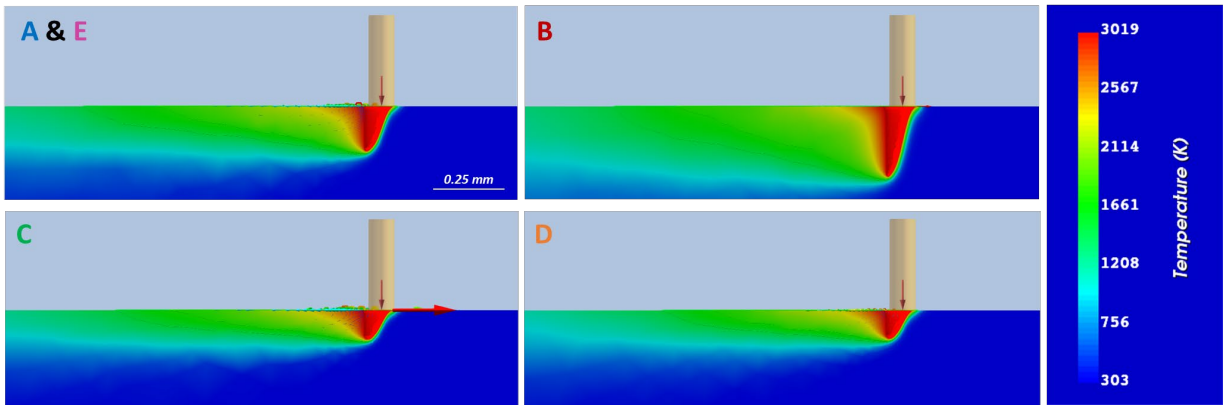


**Figure 3: Thermo-Calc AM module simulations of single raster tracks for each parameter set.**

## 3.2. As-built microstructure

### 3.2.1. Characterization of as-built microstructures

In contrast to modelling predictions, SEM BSE imaging shows the as-built microstructure did not change between parameter sets. Fine-grained α' martensite dominated the as-built material, with no discernable difference in lath size or phase content between parameter sets (Figure 4A). As-built material of all parameter sets also contained low-Z, nanoscale particles throughout the martensitic microstructure (Figure 4A). EDS mapping in Figure 5 shows these low Z-particles are enriched in Al and O, suggesting they are $Al_2O_3$ or similar compound. The origin of these particles is unknown. Atomic clustering during material deposition could explain the formation of these Al- and O-rich particles, though the size of these particles makes this somewhat unlikely. $Al_2O_3$ particles could also originate from contamination at some point in the manufacturing process (e.g., remelted chunks from a ceramic recoater blade powder coating), although this is also unlikely due to how dispersed these particles are throughout *all* specimens. No obvious partitioning of other solute elements was observed in the as-built microstructure, suggesting minimal partitioning during solid state transformations.

Martensitic laths and low Z-particles are housed within as-solidified columnar parent grains contained within larger melt pool geometries (Figure 4A). Evidence of a cellular solidification structure is periodically observed in all parameter sets, with an example highlighted in Figure 4B. Here, Ni has partitioned into austenite surrounding an α-ferrite core during cooling in the build process [32–35]. Local Ni enrichment increases the stability of the nano-scale austenite cell-walls, retaining the phase to lower temperatures. Interestingly, no clear evidence of δ-ferrite

solidification is observed in the as-built microstructure. A lack of skeletal structures or local Cr-enrichment suggests δ-ferrite microstructures are quickly consumed by austenite in the solid state, or M789 does not appreciably solidify as δ-ferrite in contrast to the simulations in Figure 2. A massive δ-ferrite to γ-austenite transformation may also occur as suggested by prior work in Fe-Ni-Cr alloys, with interesting implications on the inheritance of crystallographic orientations [36]. This and the α' martensitic transformation may also explain the limited partitioning observed in the as-built microstructure outside of the low Z-particles (Figure 5) or give new mechanistic reasons for the appearance of the low Z-particles.

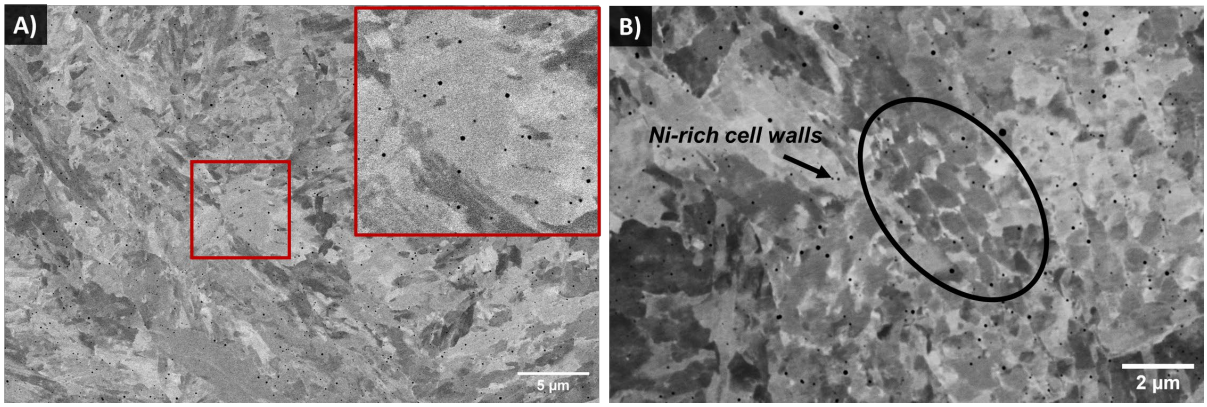


**Figure 4: Representative BSE micrographs of as-built microstructures for all parameter sets. A) Fine-grained α' martensite containing dispersed low-Z particles. B) Ni-enriched cellular structures left-over from the solidification process. Both micrographs are taken from the A parameter set with the build direction parallel to the vertical direction.**

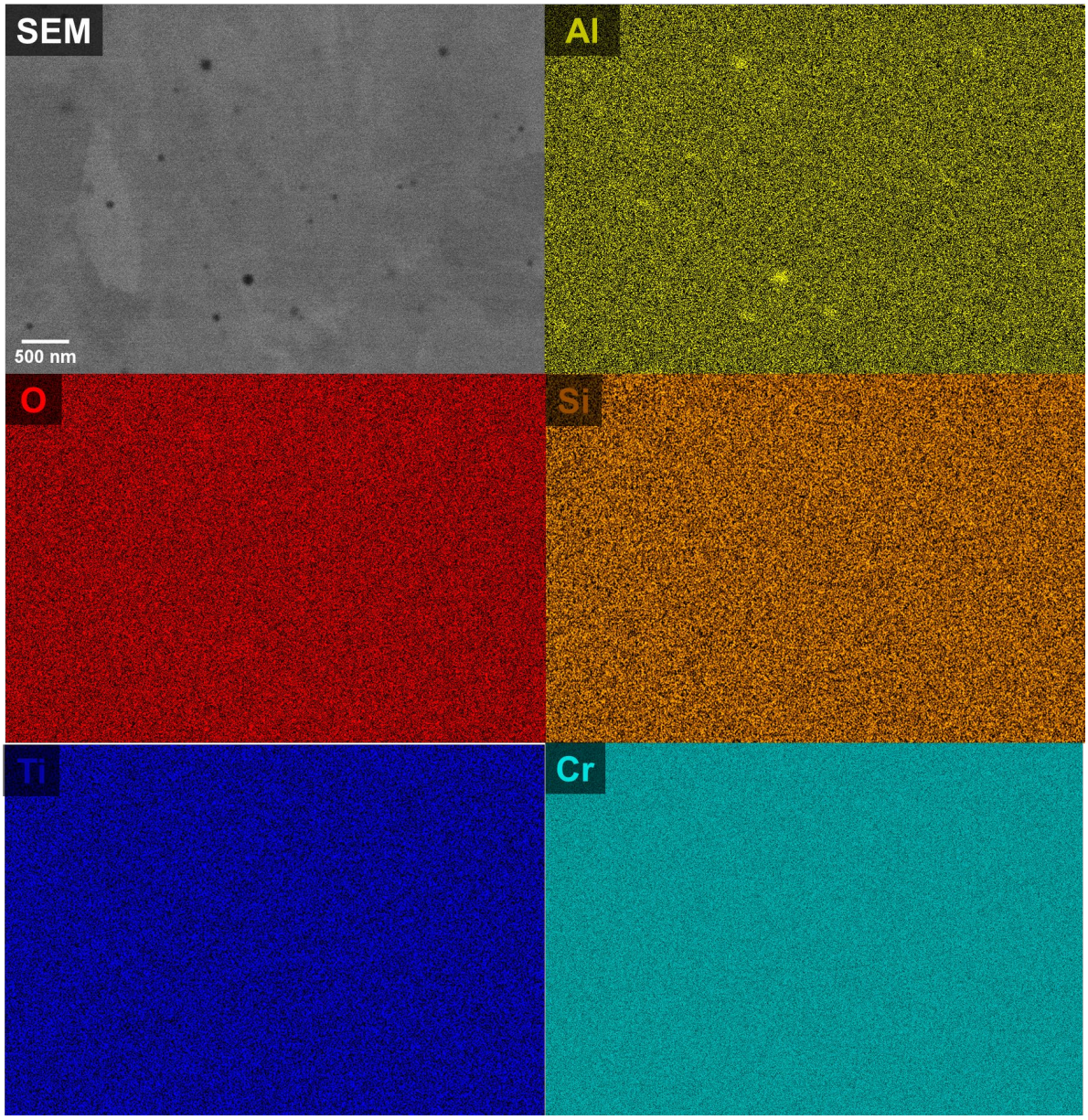


**Figure 5: BSE SEM and EDS map of the as-built low Z-particles showing Al and O enrichment. Build direction in these images is parallel to the vertical direction**

### 3.2.2. Melt pool geometries and crystallographic orientation

The consistency of as-built microstructures across parameter sets suggests M789 is resistant to changes in build parameters. Both solidification and traces of the solid-state microstructures were consistent across the varying thermal conditions manifested by the different parameter sets. This makes M789 a potentially useful alloy system for metal AM, capable of obtaining the same as-built microstructure from phase transformations relatively insensitive to thermal history. This is in stark contrast to most other metallic alloys (e.g., Ti-6Al-4V) which are highly sensitive to changes in build parameters and build process [37,38]. It's important to note defect

structures are not considered here and are discussed later in this work. It's also important to note that only the primary variables of laser power and scan speed were altered. Changes to laser spot size or more drastic changes to scan strategy (e.g. [39]) were not explored in this work.

Though the solidification and solid-state microstructures did not change between parameter sets, clear variation in melt pool geometry can be seen in Figure 6. Parameter sets A & E exhibit comparable melt pool sizes given their similar melt pools during steady state deposition. The effect of changing scan rotation angle is evident between A & E however, with the melt pools in parameter set E stacking on-top of each other and creating clearer columnar morphologies. This morphology did not have an observable impact on the solid-state microstructure. Melt pool sizes in parameter sets B, C, and D are less obvious in BSE imaging, though the orientation of parent columnar grains suggests they are in line with those predicted in Figure 3. Although the overall microstructure remains the same, different fatigue and impact resistance properties would be expected between parameter sets due to the change in macrostructure seen in Figure 6. Thus far, the only clear difference resulting from altering build parameters are the macrostructural changes in melt pool geometry observed in Figure 6. Though Ni-partitioning into cellular austenite structures could be leveraged as Ni-sources for non-equilibrium precipitation, this was not unique to any parameter set.

Crystallographic orientation was next analyzed to observe any local impact of build parameters on the as-built M789 material. Crystallographic orientations also showcase an influence of solidification microstructures on the as-built microstructure, elucidating information hidden from non-crystallographically based characterization.

Figure 7 illustrates large area EBSD inverse pole figure (IPF) maps of all five parameter sets. Each map shows a randomly textured material with no preferential orientations, again suggesting M789's microstructural evolution is largely insensitive to changes in thermal history from different build parameters. This was especially true with parameter set E where a crystallographically textured material was expected from the stacked melt pools. The lack of any crystallographic texture suggests the martensitic transformation protects as-built M789 from preferential orientations manifesting. It is also possible this phase transformation hides differences in the solidification microstructure, but characterization results so far suggest this is not the case. No detected γ-austenite survived the data cleaning process, confirming retained volumes of this phase are less than 30 nm to 50 nm in size.

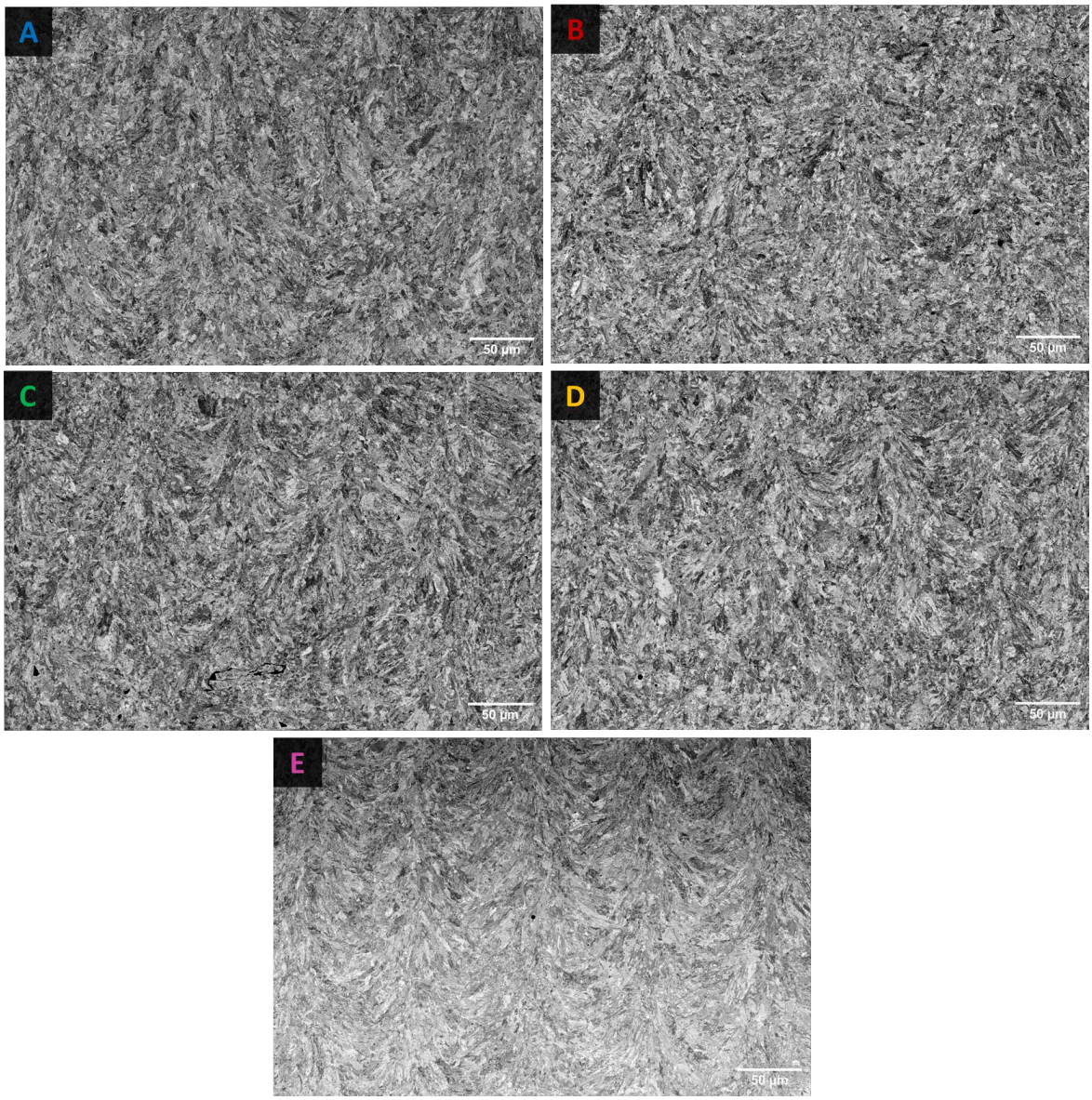


**Figure 6: BSE imaging of as-built melt pool geometries for all parameter sets. Variable melt pool geometries are observed between parameter sets as expected from Figure 3. All images are contrast boosted to highlight melt pool geometries. Build direction in all images is parallel to the vertical direction.**

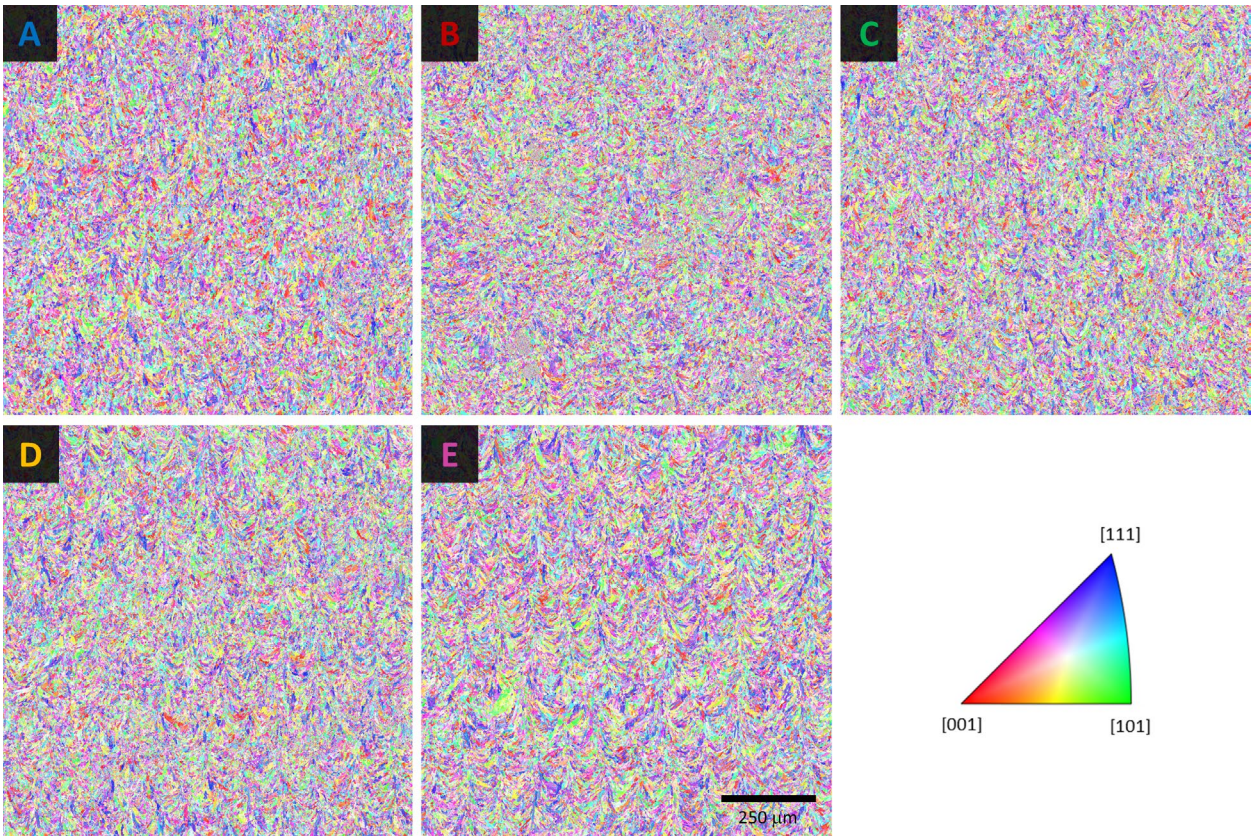


**Figure 7: EBSD IPF maps of as-built M789 for all parameter sets. Consistent orientations can be seen across all parameters, suggesting the same microstructural evolution during deposition. All orientations are colored with respect to the build direction (vertical direction).**

Further confirming the non-textured condition of the as-built microstructure are the pole figures in Figure 8. Here, α' martensite is shown to have an effectively random texture at 1× - 1.5× multiples of uniform random distribution (m.u.r.d.). Despite these low intensities, the pole figures also exhibited weak (001) and (111) fiber textures around the build direction. Such fiber textures stem from the OR's between the parent γ-austenite and α'-martensite (likely the Kurdjumov-Sachs (KS) or Nishiyama-Wasserman (NW) OR's) and a large number of γ-austenite parent grains with a (110) texture oriented along the build direction. This confirms that the solidification process of M789 is mostly unchanged in the parameter space tested here, and that a finer γ-austenite grain size had to exist for the fiber textures to form. Pole figure orientations also suggest the parent γ-austenite was the same for all parameter sets, again suggesting minimal influence of build parameters on the solidification microstructure.

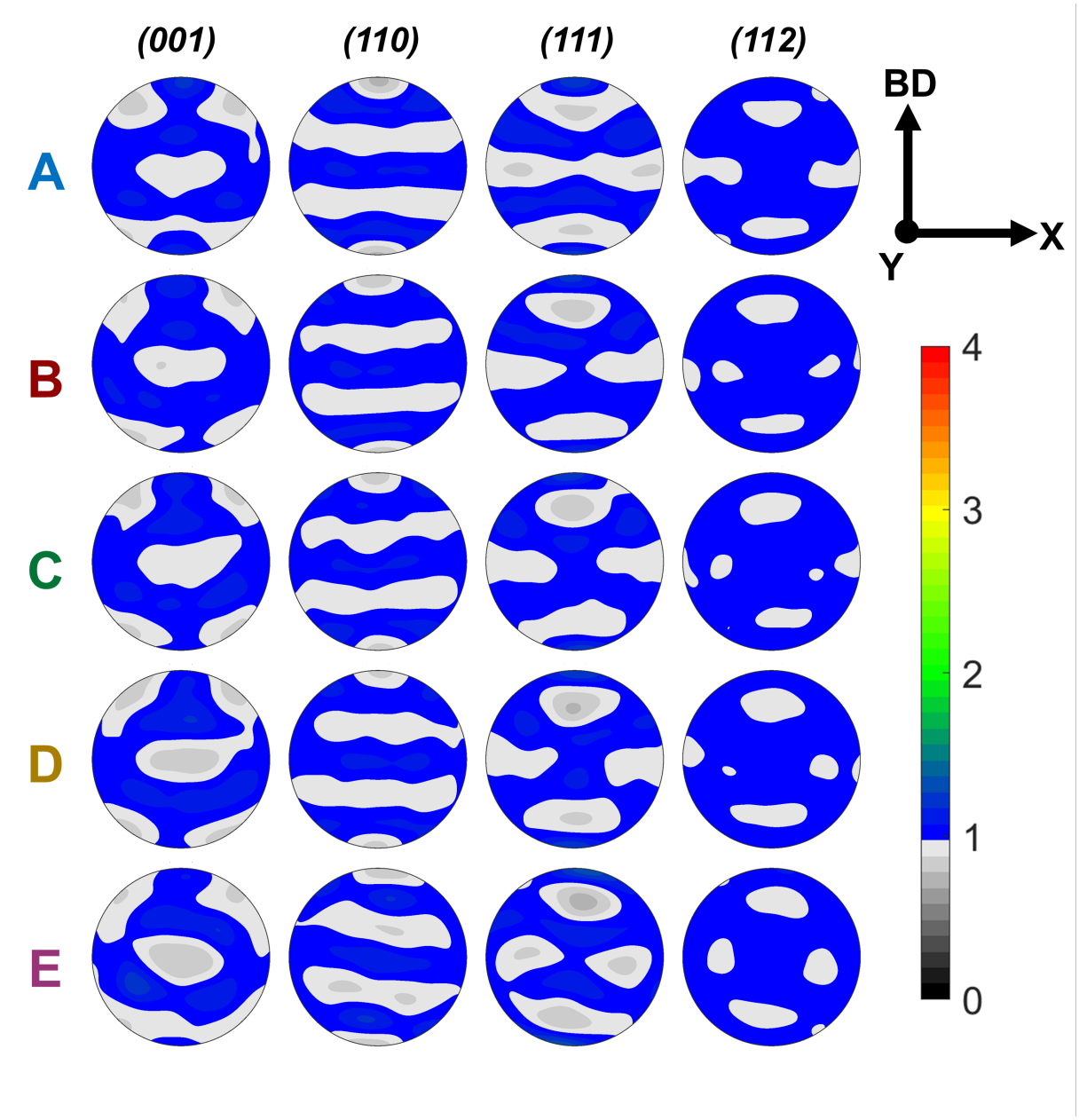


**Figure 8: α' martensite pole figures for all as-built microstructures. The low intensity fiber textures confirm there is no preferential orientation in the solid-state microstructure and that many finer γ-austenite grains had to exist with a common (110) texture along the build direction.**

Reconstruction of the parent γ-austenite phase in parameter set A was completed to complement Figure 7 and Figure 8. Reconstructed IPF maps are presented in Figure 9 for the KS, NW, and Pitsch-Petch (PP) OR's. As predicted from Figure 10, reconstructing the microstructures in Figure 11A & B produces a weakly textured parent γ-austenite microstructure consisting of columnar grains contained within prior melt pool geometries (Figure 11C-E). As

suggested by the IPF coloration, pole figures of the reconstruction reveal a (110) texture along the build direction. Whether this orientation is inherited from (001) oriented δ-ferrite solidification or during direct γ-austenite solidification is unknown. How δ-ferrite transfers its solidification orientation into γ-austenite via martensitic or massive transformations is also unknown.

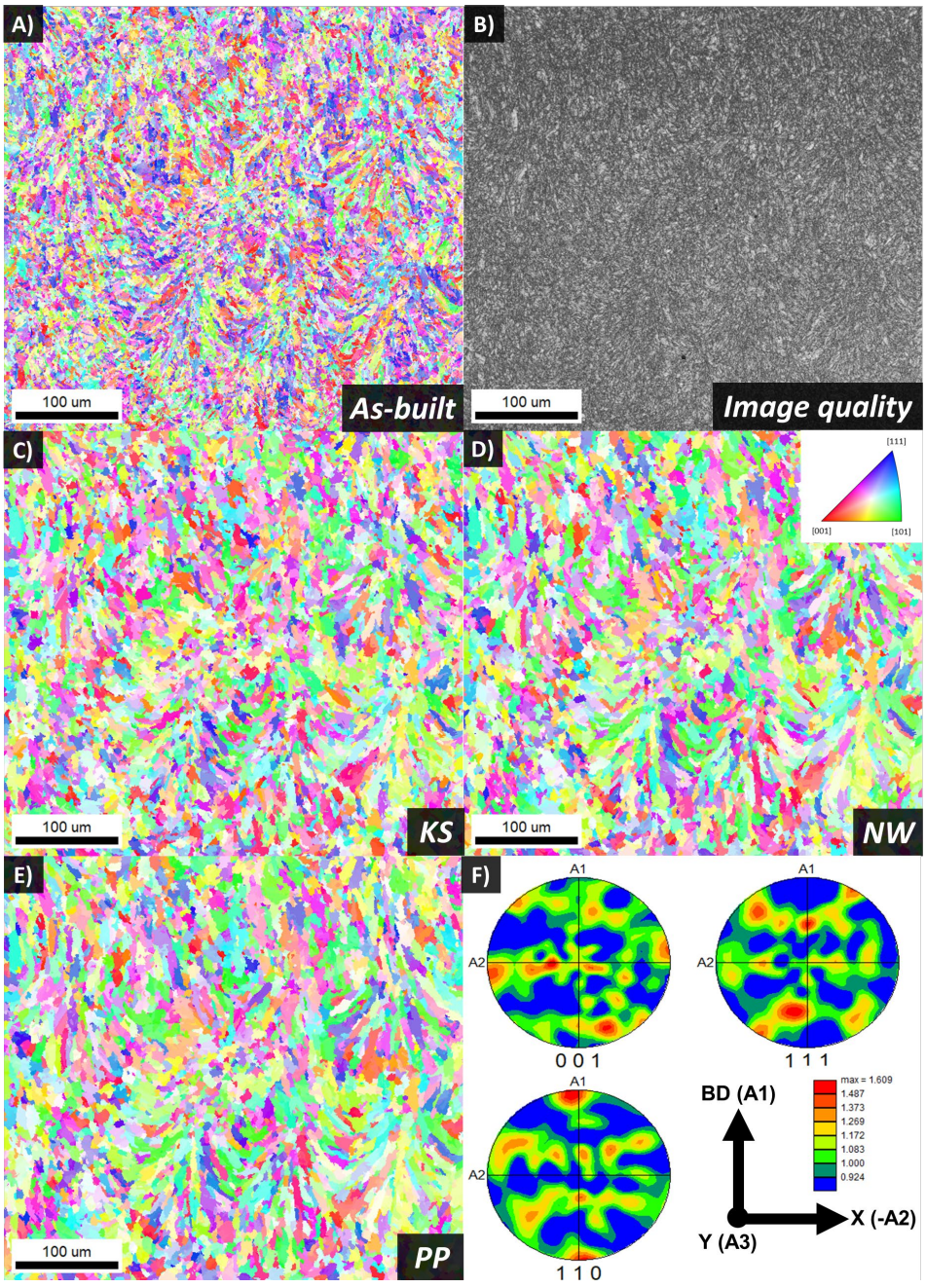


**Figure 9: Reconstruction of parent γ-austenite in parameter set A. A) As-built IPF map of α' martensite. B) As-built image quality map. C-E) Reconstructed γ-austenite microstructures using the KS, NW, and PP OR's respectively. F) Pole figures for the KS OR reconstruction showing a (110) texture along the build direction as**

**suggested by the textures in Figure 10. All orientations are colored with respect to the build direction (vertical direction).**

It remains unclear from Figure 9 which of the possible OR's dominates the γ-austenite to α' martensite transformation. Nearly equivalent parent microstructures were produced from different OR's, suggesting multiple OR's may be operating depending on local conditions.
Small-scale EBSD of parameter set A in Figure 10A was able to detect trace amounts of γ-austenite with sufficient signal to survive data processing (Figure 10B). These clusters of retained austenite were used to spot check the γ-austenite reconstructions and ascertain if one specific OR was most effective. The reconstructed microstructures in Figure 10C-E suggest there is no obviously dominant OR, with reasonable reconstructions of the local γ-austenite grain structure generated by all three tested OR's. Further work is recommended in this area.

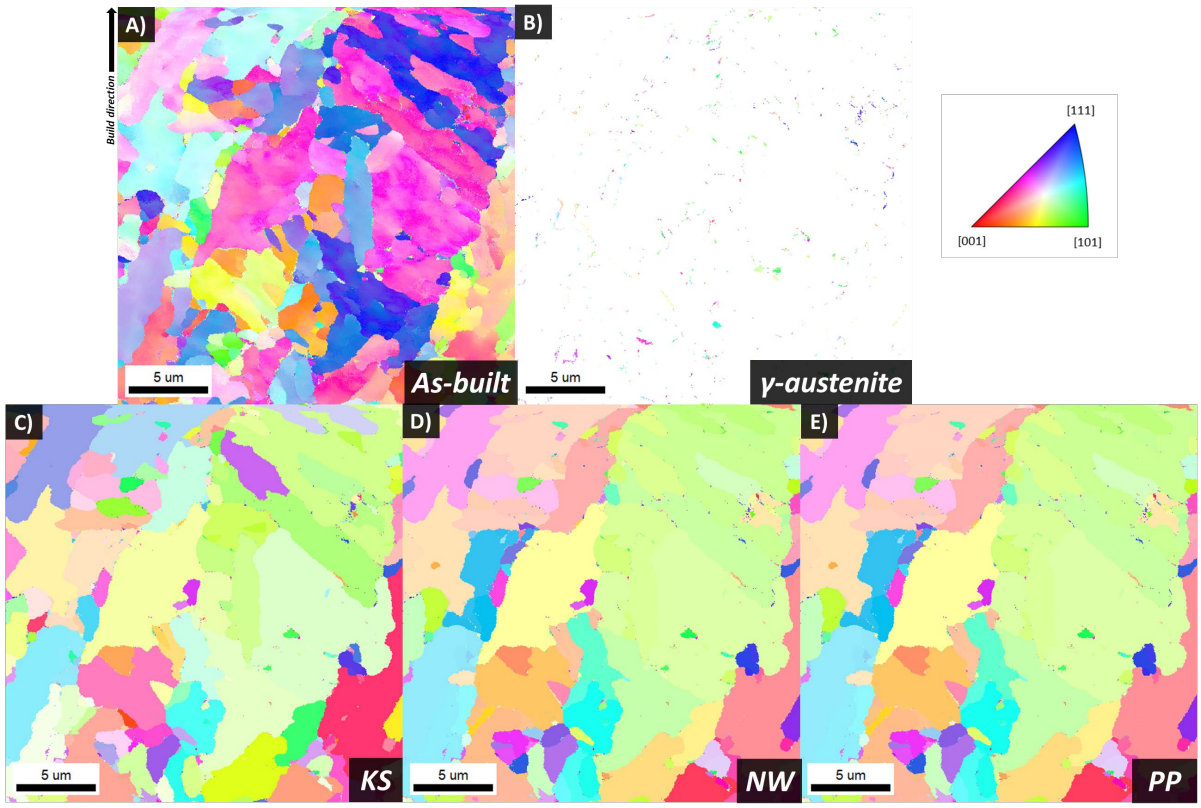


**Figure 10: Small-scale, high-resolution EBSD of the as-built microstructure from parameter set A. A) Combined α' martensite and γ-austenite IPF map. B) γ-austenite orientations from A). C-E) Reconstructed γ-austenite orientations using the KS, NW, and PP OR's respectively. All orientations are colored with respect to the build direction (vertical direction).**

### 3.2.3. X-ray diffraction

To further understand how tolerant the M789 microstructure is to the different build parameters tested here, XRD was employed to measure phase fractions in the as-built specimens. The results

of this analysis are included in Figure 11 and show the as-built phases are consistent between parameter sets. As expected from SEM imaging, the majority of the as-built microstructure consists of α' martensite. An unexpectedly high percentage of retained γ-austenite (10 % - 20 % estimated from Rietveld refinement) was also detected, suggesting the cellular structures in Figure 4B are more prevalent than observed in SEM/EBSD. Regardless, the presence of retained γ-austenite likely contributes to the large post-uniform ductility observed in prior M789 studies [19,32].

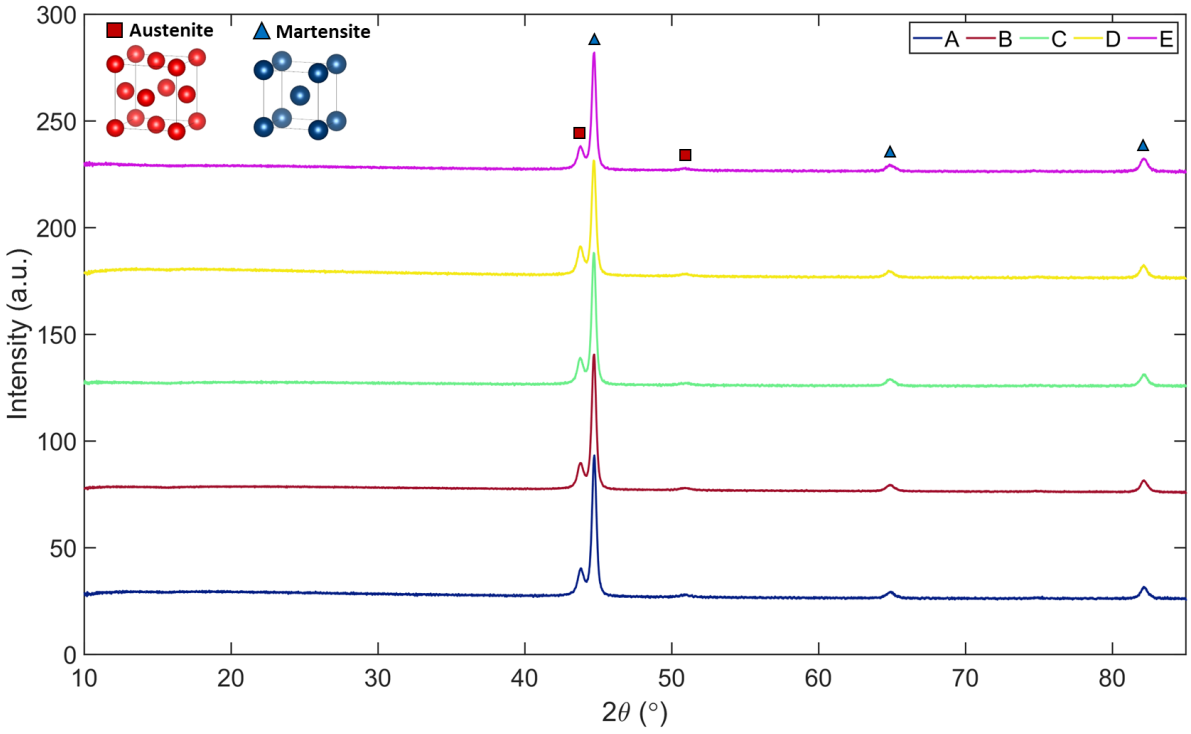


**Figure 11: XRD peak profiles of as-built material. Only α' martensite and γ-austenite peaks were observed, with comparable intensities between all parameter sets. Crystal structures were generated via the program Vesta.**

### 3.2.4. As-built hardness

Vickers hardness tests were conducted to ascertain if any one build parameter set created as-built material with an inherent improvement in hardness. Vickers hardness testing results showed the near-nominal parameter sets A & E produced the highest as-built hardness in the 340-350 HV range (Figure 12). The parameter sets B, C, and D all had statistically lower hardnesses than A & E. The differences between parameter sets also suggests that parameter sets A and E are best for future studies given the desire for higher and consistent hardness in maraging steel applications.

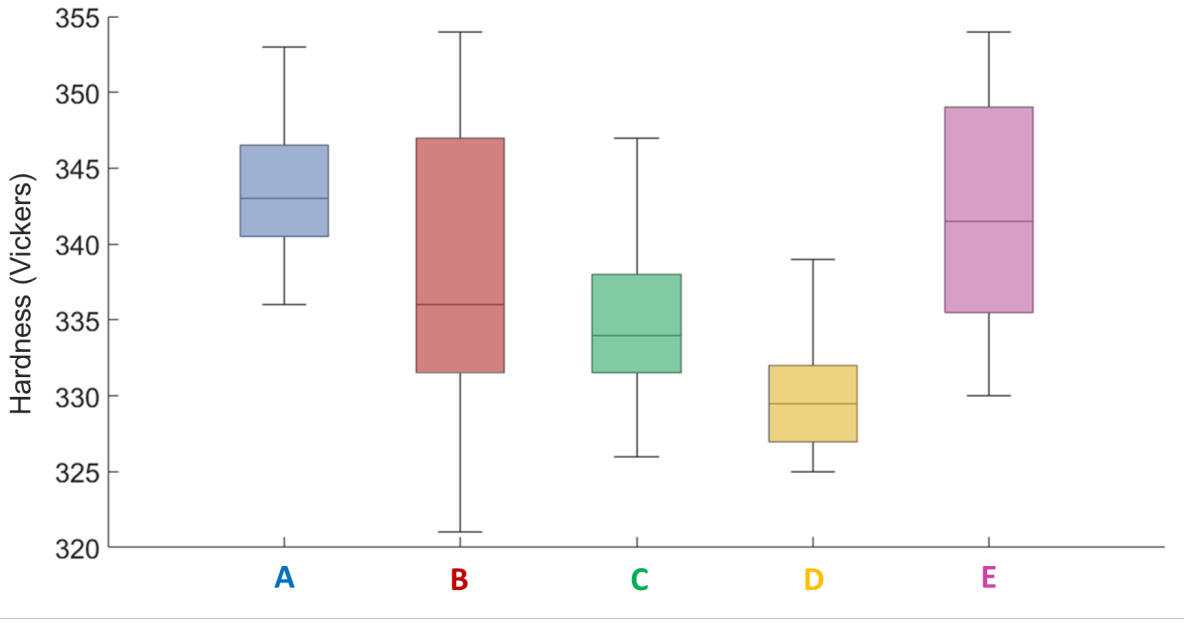


**Figure 12: Vickers hardness values for each parameter set.**

### 3.2.5. Uniaxial tensile behavior via true-stress true strain measurements

Strengths of approximately 1 GPa are consistently achieved with parameter sets A and E (Table 3). It is worth noting comparable ultimate tensile strengths, shown in Table 3, to AM as-built C300 maraging steel (966 MPa to 1058 MPa) are achieved [40]. Thus, demonstrating Co-free, Cr-containing alloys can reach performance parity with some existing maraging steels in the as-built condition. The mechanical properties reported here are similar to other M789 studies, showing the alloy's as-built mechanical response is consistent across build processes [19,41,42]. This finding is again attributed to the characteristics of the solid-state phase transformations in M789, underscoring the importance of more research in this area. The dominance of as-built defects on tensile properties makes deducing any mechanical benefits from the different parameter sets difficult. No significant tensile property differences are expected given the consistent solid-state microstructures and phase fractions. However, analysis of the work hardening behavior was completed to elucidate any hidden benefits of each parameter set prior to necking of the tensile specimen. These calculated results are presented in Figure 13 with the true-stress true-strain curves of the tested material for each parameter set.

**Table 3: Summary of ultimate tensile strengths (UTS). 1σ is standard deviation.**

| Parameter Set | UTS (MPa) ± 1σ |
|---|---|
| **A** | 1041 ± 11.4 |
| **B** | 997.7 ± 14.6 |
| **C** | 942 ± 53.7 |
| **D** | 926.2 ± 73.4 |
| **E** | 1033.7 ± 9.1 |

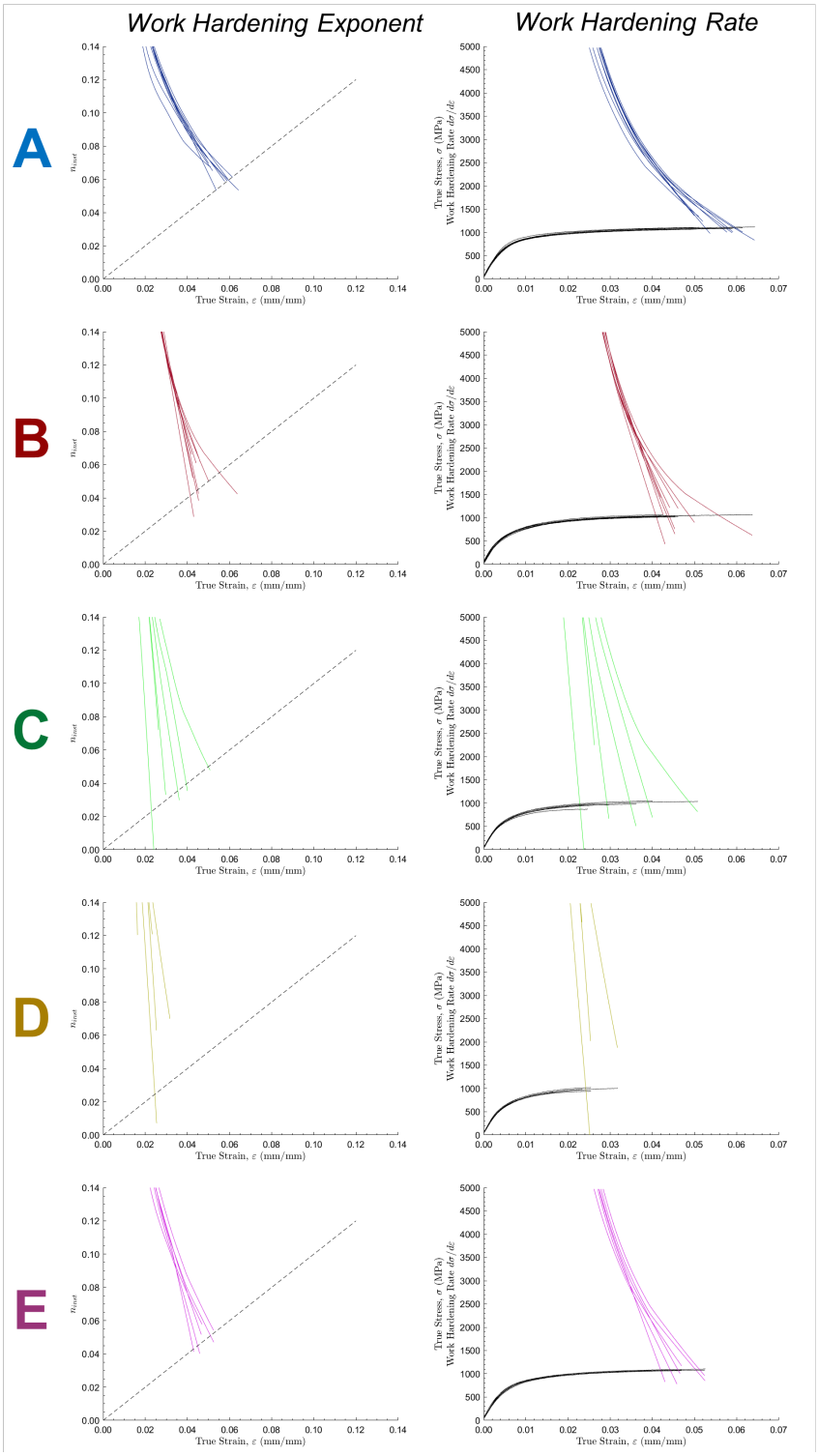


**Figure 13: Work hardening exponent and rate calculations for each parameter set. Note the significant difference in true stress-strain curves due to the greater defect density in parameter sets B, C, and D.**

## 4. Summary

Future work such involving hot isostatic pressing (HIP), a commonly applied post-build processing strategy in modern metal-based AM, will be pursued. M789 already has established heat treatments for achieving industrially desirable hardness and tensile strengths [24,43]. However novel heat treatments may expand the use of Co-free, Cr-containing maraging steels by leveraging the phase transformation behavior in the non-equilibrium solidified as-built material.

A strong case can also be made for further studying why M789 is so microstructurally resilient to significant changes in thermal history. Specifically, understanding the transformation between δ-ferrite and γ-austenite and this processes influence on the formation of α' martensite is needed to identify if build parameters can at all be used to tweak as-built microstructures. Such knowledge can also be useful for designing other build parameter tolerant alloys and developing new alloys for widespread AM applications.

The Co-free, Cr-containing maraging steel M789 proved resilient to microstructural changes induced by altering PBF-LB build parameters. As-built microstructure, phase fractions, and crystallographic orientations were similar between parameter sets. As-built M789 hardness and tensile properties did reach equivalence with as-built C300, demonstrating that Co-free, Cr-containing alloys can already achieve similar performance to Co-containing maraging steels in the as-built condition. Future work is also recommended aimed at understanding the solid-state transformations in M789 via different heat treatment strategies.

## 5. References

[1] S. Floreen, The physical metallurgy of maraging steels, Metall. Rev. 13 (1968) 115–128. https://doi.org/10.1179/mtlr.1968.13.1.115.

[2] B.-Z. Weiss, Maraging Steels - Structure, Properties, and Applications, in: Spec. Steels Hard Mater., Elsevier, 1983: pp. 35–54. https://doi.org/10.1016/B978-0-08-029358-5.50009-4.

[3] A. Gemperle, J. Gemperlová, W. Sha, G.D.W. Smith, Aging behaviour of cobalt free chromium containing maraging steels, Mater. Sci. Technol. 8 (1992) 546–554. https://doi.org/10.1179/mst.1992.8.6.546.

[4] F. Habiby, A. ul Haq, A.Q. Khan, The Properties and Applications of 18% Nickel Maraging Steels, Mater. Technol. 9 (1994) 246–252. https://doi.org/10.1080/10667857.1994.11785084.

[5] L.J. Pionke, K.C. Garland, Evaluation of shuttle solid rocket booster case materials, Natl. Aeronaut. Sp. Admninistration. (1973).

[6] W. Sha, A. Cerezo, G.D.W. Smith, Phase chemistry and precipitation reactions in maraging steels: Part I. Introduction and study of Co-containing C-300 steel, Metall. Trans. A. 24 (1993) 1221–1232. https://doi.org/10.1007/BF02668190.

[7] W. Sha, A. Cerezo, G.D.W. Smith, Phase chemistry and precipitation reactions in maraging steels: Part II. Co-free T-300 steel, Metall. Trans. A. 24 (1993) 1233–1239. https://doi.org/10.1007/BF02668191.

[8] W. Sha, A. Cerezo, G.D.W. Smith, Phase chemistry and precipitation reactions in maraging steels: Part III. Model alloys, Metall. Trans. A. 24 (1993) 1241–1249. https://doi.org/10.1007/BF02668192.

[9] M.N. Rao, Progress in understanding the metallurgy of 18% nickel maraging steels, (2006).

[10] W. Sha, A. Cerezo, G.D.W. Smith, Phase chemistry and precipitation reactions in maraging steels: Part IV. Discussion and conclusions, Metall. Trans. A. 24 (1993) 1251–1256. https://doi.org/10.1007/BF02668193.

[11] D.M. Vanderwalker, The precipitation sequence of Ni3Ti in Co-free maraging steel, Metall. Mater. Trans. A. 18 (1987) 1191–1194. https://doi.org/10.1007/BF02647188.

[12] C.F. Hickey, W. Dix, D. Kagan, Mechanical Property Characterization of VascoMax T-250, 1989.

[13] W. Sha, G.D.W. Smith, Atom Probe Studies of Early Stages of Precipitation Reactions in Maraging Steels II. Ti-Free Model Alloys and Co-Free T-300 Steel, Scr. Metall. Mater. 26 (1992).

[14] Mineral commodity summaries 2024, 2024. https://doi.org/10.3133/mcs2024.

[15] A Federal Strategy to Ensure Secure and Reliable Supplies of Critical Minerals, 2018.

[16] Directive (EU) 2022/431 of the European Parliament and of the Council of 9 March 2022 amending Directive 2004/37/EC on the protection of workers from the risks related to exposure to carcinogens or mutagens at work. PE/89/2021/REV/2. OJ L 88, 16.3.2022, p, (n.d.). http://data.europa.eu/eli/dir/2022/431/oj.

[17] C.F. Hickey, Mechanical Property Characterization of VascoMax T-250, US Army Laboratory Command, 1986.

[18] European Chemicals Agency, Substance Infocard: Cobalt. EC / List no.: 231-158-0, CAS no.: 7440-48-4, Mol. Formula: Co., (n.d.). https://www.echa.europa.eu/substance-information/-/substanceinfo/100.028.325 .

[19] Y.Z. Lek, C. Wang, X. Shen, Z. Chen, U. Ramamurty, K. Zhou, Additive manufacturing of corrosion-resistant maraging steel M789 by directed energy deposition, Mater. Sci. Eng. A. 857 (2022) 144032. https://doi.org/10.1016/j.msea.2022.144032.

[20] Y.Z. Lek, S. Gao, X. Shen, A. Jarlöv, T. Cailloux, Z. Zeng, S.M.L. Nai, K. Zhou, In-situ alloying of maraging steel with enhanced mechanical properties and corrosion resistance by laser directed energy deposition, Mater. Sci. Eng. A. 911 (2024) 146898. https://doi.org/10.1016/j.msea.2024.146898.

[21] Y. Matsukawa, T. Takeuchi, Y. Kakubo, T. Suzudo, H. Watanabe, H. Abe, T. Toyama, Y. Nagai, The two-step nucleation of G-phase in ferrite, Acta Mater. 116 (2016) 104–113. https://doi.org/10.1016/j.actamat.2016.06.013.

[22] M. Yang, D.J.M. King, I. Povstugar, Y. Wen, J. Luan, B. Kuhn, Z. Jiao, C. Wang, M.R. Wenman, X. Liu, Precipitation behavior in G-phase strengthened ferritic stainless steels, Acta Mater. 205 (2021) 116542. https://doi.org/10.1016/j.actamat.2020.116542.

[23] Y. Tian, R. Palad, L. Jiang, T. Dorin, K. Chadha, C. Aranas, The effect of heat treatments on mechanical properties of M789 steel fabricated by laser powder bed fusion, J. Alloys Compd. 885 (2021) 161033. https://doi.org/10.1016/j.jallcom.2021.161033.

[24] K. Nyamuchiwa, Y. Tian, K. Chadha, C. Aranas, Laser Powder Bed Fusion of M789 Steel on Wrought N709 Steel Substrate, in: Metallurgy and Materials Society of CIM (Ed.), Springer International Publishing, Cham, 2023: pp. 9–14. https://doi.org/10.1007/978-3-031-17425-4_2.

[25] M. Gäumann, C. Bezençon, P. Canalis, W. Kurz, Single-crystal laser deposition of superalloys: Processing-microstructure maps, Acta Mater. 49 (2001) 1051–1062. https://doi.org/10.1016/S1359-6454(00)00367-0.

[26] W. Kurz, B. Giovanola, R. Trivedi, Theory of Microstructural Development During Rapid Solidification, Acta Metall. 34 (1986) 823–830.

[27] B.H. Toby, R.B. Von Dreele, GSAS-II : the genesis of a modern open-source all purpose crystallography software package, J. Appl. Crystallogr. 46 (2013) 544–549. https://doi.org/10.1107/S0021889813003531.

[28] ASTM International (E8), ASTM E8 - Standard Test Methods for Tension Testing of

Metallic Materials, in: West Conshohocken, PA, 2016. https://doi.org/10.1520/E0008_E0008M-16A.

[29] N. Derimow, J.T. Benzing, H. Joress, A. McDannald, P. Lu, F.W. DelRio, N. Moser, M.J. Connolly, A.I. Saville, O.L. Kafka, C. Beamer, R. Fishel, S. Sarker, C. Hadley, N. Hrabe, Microstructure and mechanical properties of laser powder bed fusion Ti-6Al-4V after HIP treatments with varied temperatures and cooling rates, Mater. Des. 247 (2024) 113388. https://doi.org/10.1016/j.matdes.2024.113388.

[30] S.A. David, J.M. Vitek, R.W. Reed, T.L. Hebble, Effect of rapid solidification on stainless steel weld metal microstructures and its implications on the Schaeffler diagram, 1987. https://doi.org/10.2172/5957599.

[31] O. DeNonno, A. Saville, J. Benzing, J. Klemm-Toole, Z. Yu, Solidification behavior and texture of 316L austenitic stainless steel by laser wire directed energy deposition, Mater. Charact. 211 (2024) 113916. https://doi.org/10.1016/j.matchar.2024.113916.

[32] Z. Brytan, M. Król, M. Benedyk, W. Pakieła, T. Tański, M.J. Dagnaw, P. Snopiński, M. Pagáč, A. Czech, Microstructural and Mechanical Properties of Novel Co-Free Maraging Steel M789 Prepared by Additive Manufacturing, Materials (Basel). 15 (2022) 1734. https://doi.org/10.3390/ma15051734.

[33] M. Zanni, M. Pellizzari, A. Fortunato, A. Morri, L. Ceschini, Effect of heat treatment on microstructure and mechanical properties of a Fe-12.2Cr-10Ni-1Mo-1Ti-0.6Al precipitation hardening-stainless steel manufactured via laser powder bed fusion, Prog. Addit. Manuf. (2024). https://doi.org/10.1007/s40964-024-00854-z.

[34] A. Santana, A. Eres-Castellanos, J.D. Poplawsky, D. San-Martin, J.A. Jimenez, E. Urones-Garrote, A.J. Clarke, C. Capdevila, F.G. Caballero, Solute and phase heterogeneous distribution at different scales and its effect on ageing physical phenomena in a laser powder bed fusion produced maraging steel, Addit. Manuf. 94 (2024) 104494. https://doi.org/10.1016/j.addma.2024.104494.

[35] D. Ordnung, T. Mertens, J. Tacq, M.H. Nasab, M. Sinico, G. Li, L. Thijs, B. Vrancken, B. Van Hooreweder, Enhancing fatigue life of as-printed martensitic M789 steel produced by laser powder bed fusion via in-process surface integrity improvement and phase change induced compressive residual stresses, Addit. Manuf. 88 (2024) 104263. https://doi.org/10.1016/j.addma.2024.104263.

[36] S. Laliberté-Riverin, S.R. Yassine, E. Mena-Morcillo, K. Sanni, M. Cova, M. Hassanipour, P.R. Provencher, J. Mauzeroll, M. Brochu, Microstructure, corrosion behavior, and fatigue resistance of laser powder bed fusion-produced precipitation-hardening martensitic M789 stainless steel, Surfaces and Interfaces. 45 (2024) 103830. https://doi.org/10.1016/j.surfin.2023.103830.

[37] A.I. Saville, J.T. Benzing, S.C. Vogel, J. Buckner, C. Donohoue, A.B. Kustas, A. Creuziger, K.D. Clarke, A.J. Clarke, Schmid factor crack propagation and tracking crystallographic texture markers of microstructural condition in direct energy deposition additive manufacturing of Ti-6Al-4V, Addit. Manuf. 58 (2022) 103023.

https://doi.org/10.1016/j.addma.2022.103023.

[38] A.I. Saville, S.C. Vogel, A. Creuziger, J.T. Benzing, A.L. Pilchak, P. Nandwana, J. Klemm-Toole, K.D. Clarke, S.L. Semiatin, A.J. Clarke, Texture evolution as a function of scan strategy and build height in electron beam melted Ti-6Al-4V, Addit. Manuf. 46 (2021) 102118. https://doi.org/10.1016/j.addma.2021.102118.

[39] H. Yeung, J. Chen, G. Yang, Y. Guo, D. Lin, W. Tan, J. Weaver, Effect of spiral scan strategy on microstructure for additively manufactured stainless steel 17–4, Manuf. Lett. 29 (2021) 1–4. https://doi.org/10.1016/j.mfglet.2021.04.005.

[40] J. Vishwakarma, K. Chattopadhyay, N.C. Santhi Srinivas, Effect of build orientation on microstructure and tensile behaviour of selectively laser melted M300 maraging steel, Mater. Sci. Eng. A. 798 (2020) 140130. https://doi.org/10.1016/j.msea.2020.140130.

[41] Y. Tian, R. Palad, C. Aranas, Microstructural evolution and mechanical properties of a newly designed steel fabricated by laser powder bed fusion, Addit. Manuf. 36 (2020) 101495. https://doi.org/10.1016/j.addma.2020.101495.

[42] K. Chadha, Y. Tian, J.G. Spray, C. Aranas Jr., Role of Heat Treatment on the Texture Evolution of M789 Steel Developed by LPBF Process, Defect Diffus. Forum. 421 (2022) 3–8. https://doi.org/10.4028/p-g3lqo7.

[43] S.-C. Han, U.M. Chaudry, S.B. Cenalmor, S.M. Yeon, J. Yoon, H. Lee, K. Kim, T.-S. Jun, Effect of Heat Treatment on Corrosion and Mechanical Properties of M789 Alloy Fabricated Using DED, Metals (Basel). 13 (2023) 1214. https://doi.org/10.3390/met13071214.

[44] J. Ahrens, B. Geveci, C. Law, ParaView: An End-User Tool for Large-Data Visualization, in: Vis. Handb., Elsevier, 2005: pp. 717–731. https://doi.org/10.1016/B978-012387582-2/50038-1.

[45] N.H. Moser, A.K. Landauer, O.L. Kafka, Imppy3d: Image processing in python for 3D image stacks, Natl. Inst. Stand. Technol. Public Data Repos. (2023). https://doi.org/doi.org/10.18434/mds2-2806.

[46] A. Buades, B. Coll, J.-M. Morel, A Non-Local Algorithm for Image Denoising, in: 2005 IEEE Comput. Soc. Conf., IEEE, San Diego, CA, USA, 2005: pp. 60–65. https://doi.org/10.1109/CVPR.2005.38.

[47] T. Lewiner, H. Lopes, A.W. Vieira, G. Tavares, Efficient Implementation of Marching Cubes' Cases with Topological Guarantees, J. Graph. Tools. 8 (2003) 1–15. https://doi.org/10.1080/10867651.2003.10487582.

## Appendix A. Scanning kelvin probe force microscopy (SKPFM)

Scanning kelvin probe force microscopy (SKPFM) measurements were completed to qualitatively assess local corrosion differences in as-built material for parameter set A. SKPFM was performed with a nominal 2.8 N/m cantilever with Pt/Ir coating for conductivity and a resonance frequency of 75 kHz. SKPFM measurements were performed in double-pass, amplitude-modulation mode with a typical lift height of 5 nm compared to the tapping mode first pass. The small lift height ensured the tip was held close to the sample surface for enhanced spatial resolution and reduced long range electrostatic forces acting on the cantilever body. SKPFM data was leveled by aligning rows through a first order polynomial fitting.

SKPFM analysis and STEM imaging were both completed on build parameter set A to better understand the as-built microstructure and identify any unique characteristics useful to improving the performance of these alloys. Spatially correlated SKPFM was completed on a microstructural region previously identified by SEM BSE imaging. The two high contrast features (increased height in Figure 14B) are surface contamination whose shape and position are readily identifiable in Figure 14. The use of these fiducials (the larger of which is indicated with an arrow) show that the height maps generated from SKPFM contained cellular-like features thought to be similar to those observed in Figure 4B, lending confidence to the presence of retained γ-austenite cells throughout the microstructure.

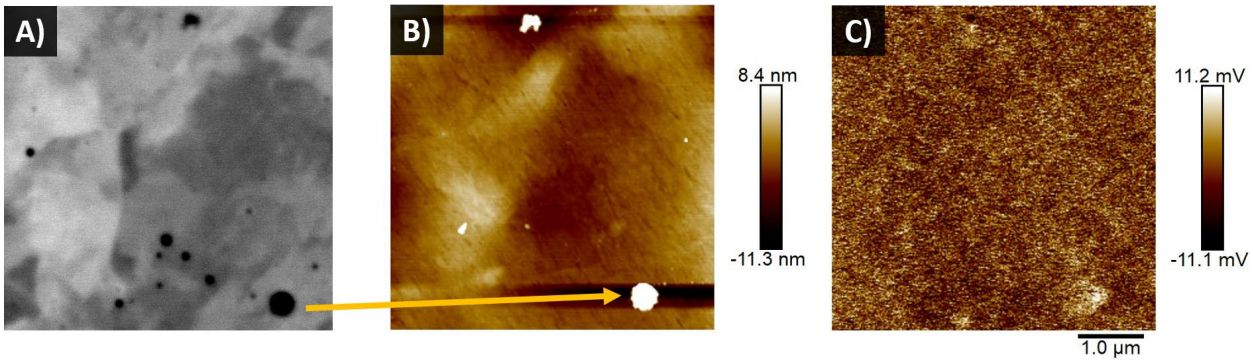


**Figure 14: SKPFM map of the as-built microstructure from build parameter set A. A) BSE SEM image of the analyzed area with low Z-particles and fiduciary features present. B) Height map from the scanned area, showing cellular-like structures not visible in BSE imaging. C) Surface potential map showing minimal-to-no change in expected corrosion behavior in the surveyed region.**

## Appendix B. X-ray computed tomography (XCT)

As-built porosity defects were characterized for Parameter sets A and C using X-ray computed tomography (XCT) with 140 kV and 80 µA on a North Star Imaging X50 machine here with 6.60 µm/pixel ± 0.33 µm/pixel spatial resolution. All XCT data was post-processed using eFX1 Software Suite Version 2.3.4 to quantify defect volume fractions and spatial distribution. Defect characterization was completed only for parameter sets A and C where defect density was expected to be the lowest and highest, respectively. Data visualization was completed using ParaView [44].

The shape of the external surfaces, as well as the internal pores, along the gauge sections of the Specimens A and C were characterized using X-ray computed tomography (XCT). The XCT measurements were performed using a North Star Imaging X50 machine. A resolution of 6.60 µm/pixel ± 0.33 µm/pixel was chosen, and the entire gauge section was imaged within a single field-of-view (FOV). Specimens A and C were measured simultaneously (in the same FOV) to reduce the acquisition time of the X-ray radiographs. X-ray transparent material (i.e., folded paper) was sandwiched between the specimens to ensure that the individual specimens could be easily separated and identified during post-processing of the reconstructed images. Reconstruction of the radiographs was also completed using North Star Imaging (proprietary) software: efX Software Suite Version 2.3.4. Additional settings used during the acquisition of the XCT radiographs can be found in Table A1.

The reconstructed images were further post-processed using IMPPY3D [45], which is an open-source Python library developed at NIST. First, the ring artifacts were removed from the grayscale images, followed by non-local means denoising [46]. Then, the images were segmented using a global threshold value, resulting in a binarized image stack where white pixels correspond to solid, metallic material. A before-and-after example of segmenting a reconstructed image is illustrated in Figure 15 .

After segmentation, the image stack was converted into a three-dimensional (3D) voxel model. Each voxel represents an extruded pixel implying an equal width, height, and length of 6.60 µm. Fully enclosed pores were identified by inverting the values of the segmented image stack. Due to the memory demand required to store so many voxels, the 3D models of Specimens A and C were transformed into surface meshes using the marching cubes algorithm [47]. Individual pores were left as voxels however. Quantitative metrics were also calculated from the segmented images, such as equivalent spherical volumes of the pores and the overall porosity of the specimens.

**Table A1: Summary of nominal XCT parameters**

| | |
|---|---|
| Accelerating voltage | 140 kV |
| Accelerating amperage | 80 µA |

| | |
|---|---|
| Radiograph exposure time | 2.5 s |
| Voxel edge length | 6.60 µm |
| Radiographs taken about 360° | 2400 |
| Num. radiographs averaged | 4 |
| Image bit depth | 14-bit |
| Thickness of copper filter | 1.27 mm |

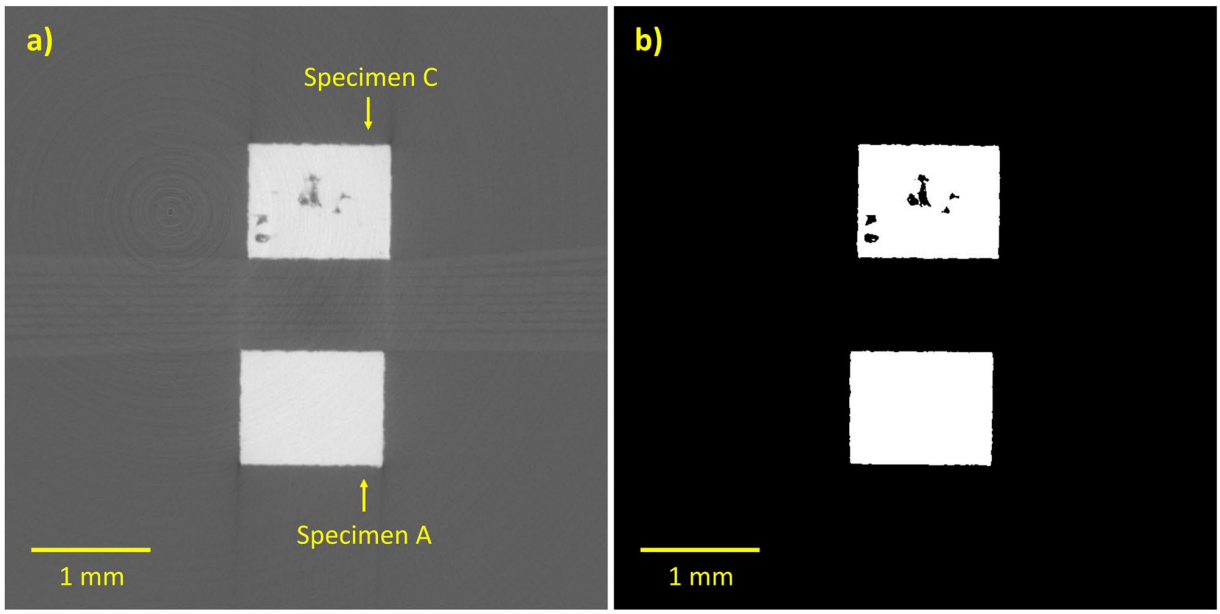


**Figure 15: Before a) and after b) images of X-ray computed tomography data processing of as-built defects.**

As-built defects were characterized in the parameter sets with the hypothesized smallest and largest defect volumes (A & C, respectively). Example as-built defects in parameter sets A (0.001 % porosity by volume) and C (0.071 % porosity by volume) are presented in Figure 16 of the gauge region of mini-tensile specimens from XCT. The effect of increased scanning speed is immediately clear between the two scans, with parameter set C having considerably larger and more frequent defects than parameter set A. These findings highlight how the mechanical performance of the as-built M789 will vary significantly between parameter sets A and C despite the as-built microstructure remaining largely the same. Parameter sets B and D also exhibited larger and more frequent defects than A or E, also likely leading to reduced mechanical performance compared to the closer-to-ideal parameter sets. Given the small sampling volume, only qualitative trends between parameter sets are discussed here.

These findings suggest that build parameter selection to minimize defects in AM builds can be prioritized when using M789. The as-built microstructure is remarkably consistent despite the large change in thermal history, potentially due to M789's low martensite start temperature and

aspects of the δ-ferrite to γ-austenite phase transformation. This finding means defect minimization can be prioritized without risking the formation of detrimental microstructures, enabling the easy manufacture of parts from this alloy across build processes and machine variants. Further work is planned to validate this idea.

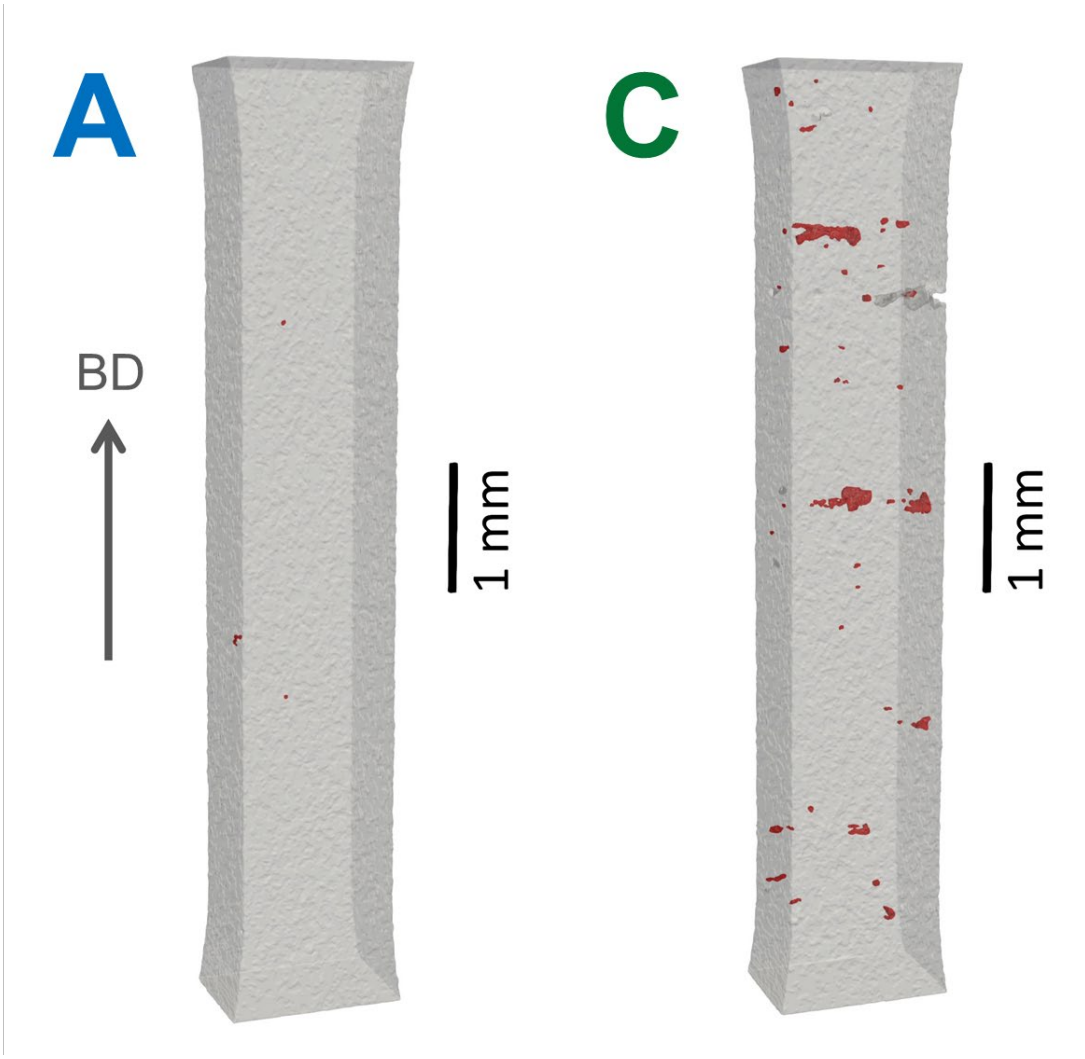


**Figure 16: XCT illustrations of defects in build parameter set A and build parameter set C. Note the build direction is parallel to the tensile direction.**